

# Measurement of the magnetic interaction between two bound electrons of two separate ions

Shlomi Kotler<sup>1†</sup>, Nitzan Akerman<sup>1</sup>, Nir Navon<sup>1†</sup>, Yinnon Glickman<sup>1</sup> & Roei Ozeri<sup>1</sup>

Electrons have an intrinsic, indivisible, magnetic dipole aligned with their internal angular momentum (spin). The magnetic interaction between two electronic spins can therefore impose a change in their orientation. Similar dipolar magnetic interactions exist between other spin systems and have been studied experimentally. Examples include the interaction between an electron and its nucleus and the interaction between several multi-electron spin complexes<sup>1–5</sup>. The challenge in observing such interactions for two electrons is twofold. First, at the atomic scale, where the coupling is relatively large, it is often dominated by the much larger Coulomb exchange counterpart<sup>1</sup>. Second, on scales that are substantially larger than the atomic, the magnetic coupling is very weak and can be well below the ambient magnetic noise. Here we report the measurement of the magnetic interaction between the two ground-state spin-1/2 valence electrons of two <sup>88</sup>Sr<sup>+</sup> ions, co-trapped in an electric Paul trap. We varied the ion separation, *d*, between 2.18 and 2.76 micrometres and measured the electrons' weak, millihertz-scale, magnetic interaction as a function of distance, in the presence of magnetic noise that was six orders of magnitude larger than the magnetic fields the electrons apply on each other. The cooperative spin dynamics was kept coherent for 15 seconds, during which spin entanglement was generated, as verified by a negative measured value of  $-0.16$  for the swap entanglement witness. The sensitivity necessary for this measurement was provided by restricting the spin evolution to a decoherence-free subspace that is immune to collective magnetic field noise. Our measurements show a  $d^{-3.0(4)}$  distance dependence for the coupling, consistent with the inverse-cube law.

Early during the twentieth century, a number of experiments indicated that the electron is more than just an electrically charged point particle. Introducing the electron spin and its accompanying magnetic moment explained a multitude of experimental observations, such as the fine-structure spectrum of hydrogen, anomalous Zeeman splitting and the famous Stern–Gerlach experiment. Since then, the magnetic field of a single electron has been detected<sup>6</sup> and its magnetic dipole measured with unprecedented accuracy<sup>7</sup>.

Because a single electron is a tiny magnet, every two electrons should influence each other's magnetic dipole orientation, just like magnets do. However, because electrons are indistinguishable particles, this interaction competes with the Coulomb spin-exchange forces which are dominant on the atomic scale. This can be resolved by increasing the inter-electron separation, *d*. Although the magnetic energy becomes dominant, it also decreases as  $d^{-3}$ . Therefore, such an approach can be fruitful only when accompanied by an appropriate increase in the magnetic dipole moment or an improvement in the measurement sensitivity. With recent advances in magnetometry on the scale of tens of nanometres, the magnetic interaction of two nitrogen–vacancy spin-1 defects in diamond has been observed to result in their entanglement<sup>4</sup>, and weak interaction strengths, as low as 60 Hz, have been measured<sup>5</sup>. A comparable magnetic interaction strength was observed between atoms in dipolar quantum gases<sup>2,3</sup>, where the magnetic dipole of each atom ranged from six to ten times that of the electron.

In this work we used two trapped <sup>88</sup>Sr<sup>+</sup> ions, each with a single valence electron and no nuclear spin<sup>8</sup>. These bound electrons inherited

the well-isolated environment of their ions along with a high degree of controllability (Methods Summary). Indeed, ions can be tightly confined and laser-cooled to their mechanical ground state<sup>9</sup>, allowing for the long interrogation times necessary for weak signal measurements. Examples include state-of-the-art detection of electric<sup>10–12</sup> and magnetic<sup>13–17</sup> fields, and the detection of gravitational time dilation<sup>18</sup>. The relative magnetic dipole correction imposed by using bound rather than free electrons is smaller than 0.0018% (ref. 19), which is well below our reported sensitivity.

We now describe the magnetic dipolar interaction and competing noise. As shown in Fig. 1a, we aligned the external magnetic field along the line connecting the two ions. The spin part of the two-ion Hamiltonian can be written as

$$H = \frac{\hbar}{2} (\omega_{A,1}\sigma_{z,1} + \omega_{A,2}\sigma_{z,2}) + 2\hbar\zeta\sigma_{z,1}\sigma_{z,2} - \hbar\zeta(\sigma_{x,1}\sigma_{x,2} + \sigma_{y,1}\sigma_{y,2}) \quad (1)$$

Here  $\hbar$  is the Planck constant divided by  $2\pi$ ;  $\sigma_{j,i}$  is the  $j \in \{x, y, z\}$  Pauli spin operator of the  $i$ th spin;  $\omega_{A,i} = g\mu_B B_i/2\hbar$  is the spin Larmor frequency, where  $B_i$ ,  $\mu_B$  and  $g$  are the external magnetic field, Bohr magneton and the electron spin gyromagnetic ratio, respectively. The spin–spin interaction strength is  $\zeta = \mu_0(g\mu_B/2)^2/4\pi\hbar d^3$ , with  $\mu_0$  the vacuum permeability constant. The first term on the right-hand side of equation (1) describes the Zeeman shift of the spins' energy due to the magnetic field. The second and third terms are due to spin–spin interactions. The second term creates a shift in the resonance frequency of one spin that is conditioned on the state of the other, and was recently measured for the case of two nitrogen–vacancy spin-1 defects<sup>4,5</sup>. The third term results in a collective spin flip in which a spin excitation is exchanged. Owing to conservation of energy, for this term to be on-resonance and effective, the two spins have to be exactly degenerate, that is,  $B$  has to be exactly uniform. It is the third term which was at the focus of our experiment.

Ultimately, the ability to measure a weak magnetic spin–spin interaction is limited by collective external magnetic field fluctuations, described by the first term in equation (1). Typical laboratory magnetic field noise amplitudes are of the order of 0.1  $\mu$ T, which is equivalent to fluctuations of a few kilohertz in  $\omega_{A,i}$  ( $i = 1, 2$ ). These are, however, six orders of magnitude greater than the spin–spin interaction strength.

A state-space solution can remedy the effect of these large magnetic fluctuations. It requires identifying a set of quantum states which are, on the one hand, sensitive to the desired signal, and, on the other hand, invariant under a certain class of noise processes. Previously this approach was used to measure magnetic field gradients<sup>13,14,16</sup> as well as narrow laser linewidths and the electric quadrupole shift of atomic transitions<sup>10</sup>. Here we tailored the states to the magnetic dipolar interaction. The four eigenstates of the Hamiltonian in equation (1) are  $|\uparrow\uparrow\rangle$ ,  $|\downarrow\downarrow\rangle$  and the two entangled Bell states  $|\Psi_{\pm}\rangle = (|\uparrow\downarrow\rangle \pm |\downarrow\uparrow\rangle)/\sqrt{2}$ . The first two eigenstates are twice as susceptible to magnetic field fluctuations than are the single-spin states, whereas the energy splitting between the latter two is  $4\hbar\zeta$  and does not depend on  $B$  at all (see Fig. 1b for an energy level diagram). By restricting the spin–spin evolution to the decoherence-free subspace

<sup>1</sup>Department of Physics of Complex Systems, Weizmann Institute of Science, Rehovot 76100, Israel. <sup>†</sup>Present addresses: Physical Measurement Laboratory, National Institute of Standards and Technology, Boulder, Colorado 80305, USA (S.K.); Cavendish Laboratory, University of Cambridge, J. J. Thomson Avenue, Cambridge CB30HE, UK (N.N.).

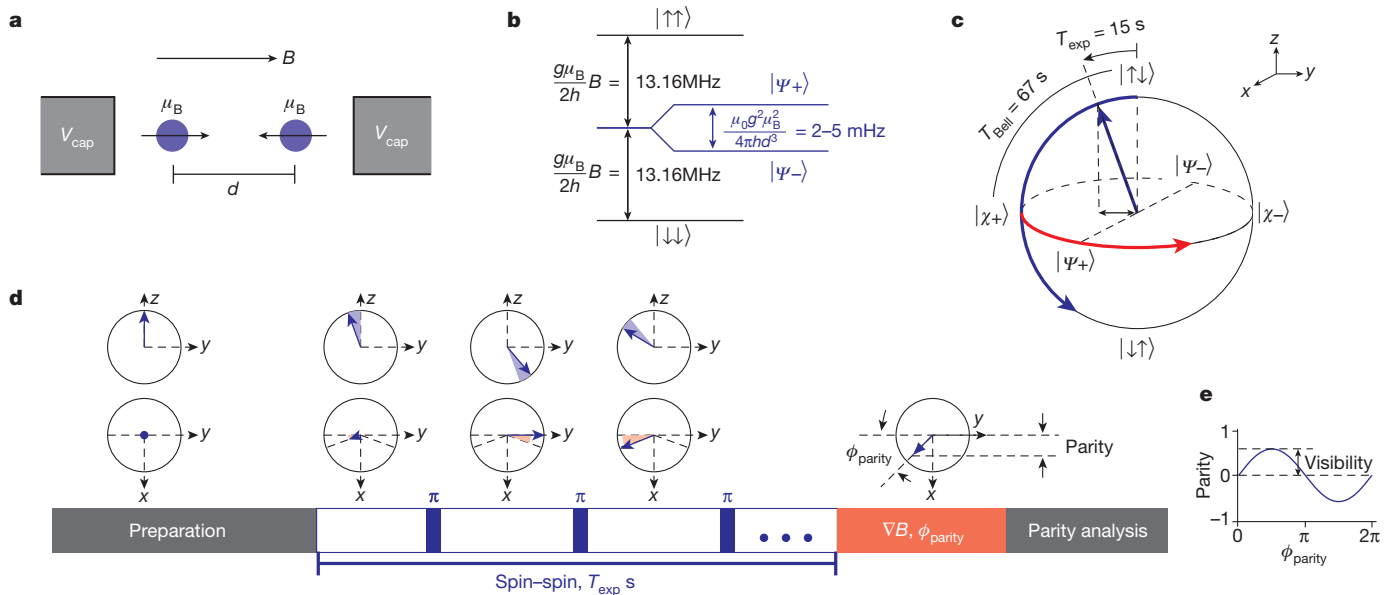


**Figure 1 | Experiment overview.** **a**, Set-up schematics. Two  $^{88}\text{Sr}^+$  ions are trapped in a linear radio-frequency Paul trap (only d.c. electrodes at potential  $V_{\text{cap}}$  are shown). **b**, Two spins' energy diagram with magnetic interaction eigenvectors  $|\Psi_{\pm}\rangle = (|\uparrow\downarrow\rangle \pm |\downarrow\uparrow\rangle)/\sqrt{2}$ . **c**, Geometric Bloch representation of the DFS.  $|\chi_{\pm}\rangle = (|\uparrow\downarrow\rangle \pm i|\downarrow\uparrow\rangle)/\sqrt{2}$ . Spin-spin interaction induces  $x$  rotation (blue arc). Magnetic field gradients generate  $z$  rotations (red arc). For  $d = 2.4\ \mu\text{m}$ , spin-spin coupling rotates  $|\uparrow\downarrow\rangle$  to the fully entangled state  $|\chi_+\rangle$  after an interaction time  $T_{\text{Bell}} = 67\text{ s}$ . Our actual experiment duration was  $T_{\text{exp}} = 15\text{ s}$ , corresponding to a  $21.6^\circ$  rotation. This angle is estimated by the parity visibility (black double arrow projection of the Bloch vector on the

equatorial plane). A collective spin flip corresponds to  $180^\circ$  rotation about  $x$ . **d**, Experimental sequence. Infinitesimal spin evolution is depicted by the shaded sectors of the  $z$ - $y$  and  $x$ - $y$  projections of the Bloch sphere. After initialization to  $|\uparrow\uparrow\rangle$ , spin-spin evolution is interrupted by equidistant collective spin flips, restricting the effect of magnetic field gradients (bottom middle three spheres). The Bloch vector continuously accumulates an angle with respect to  $z$  (upper middle three spheres). Finally, a controlled magnetic gradient rotates the Bloch vector about the  $z$  axis by  $\phi_{\text{parity}}$  radians. The projection of the final Bloch vector on the  $x$  axis corresponds to the parity observable. **e**, Parity analysis fringe example (numerical).

(DFS) spanned by  $|\Psi_{\pm}\rangle$ , it is possible to observe spin-spin interactions without susceptibility to spatially homogeneous magnetic noise.

Spin-spin interaction within the DFS takes a simple form which can be understood in terms of the geometric Bloch sphere representation shown in Fig. 1c. In this subspace, equation (1) takes the form  $H_{\text{int}} = 2\hbar\xi(|\uparrow\downarrow\rangle\langle\downarrow\uparrow| + |\downarrow\uparrow\rangle\langle\uparrow\downarrow|)$ . The  $|\Psi_{\pm}\rangle$  states are invariant under the interaction (Fig. 1b). All other states undergo rotation (Fig. 1c, solid blue arc) around the direction defined by  $|\Psi_{\pm}\rangle$ , hereafter referred to as the  $x$  direction (Fig. 1c). Starting from the north pole ( $|\uparrow\uparrow\rangle$ ), the system rotates through the fully entangled state  $|\chi_+\rangle = (|\uparrow\downarrow\rangle + i|\downarrow\uparrow\rangle)/\sqrt{2}$  and towards the south pole ( $|\downarrow\downarrow\rangle$ ).

Even in the DFS, spatial inhomogeneity in the external magnetic field can obscure the spin-spin signal. By observing the energy separation between  $|\uparrow\downarrow\rangle$  and  $|\downarrow\uparrow\rangle$  and compensating for inhomogeneities with external coils, we were able to reduce the gradients to as low as  $\nabla B = 3.57 \times 10^{-7}\text{ T m}^{-1}$  (Supplementary Information). This, however, was still strong enough to lift the degeneracy between  $|\uparrow\downarrow\rangle$  and  $|\downarrow\uparrow\rangle$  by  $\Delta\omega_A = (g\mu_B/2\hbar)(\nabla B)d = 2\pi \times 20\text{ mHz}$ , thus detuning the weak, millihertz, spin-spin coupling from resonance and resulting in the Hamiltonian  $H = H_{\text{int}} + (\hbar/2)\Delta\omega_A(|\uparrow\downarrow\rangle\langle\downarrow\uparrow| - |\downarrow\uparrow\rangle\langle\uparrow\downarrow|)$ . In geometric terms, starting at the Bloch sphere north pole, the system state is rapidly rotated by the field gradient about the  $z$  axis (Fig. 1c, red arc). This counteracts the slower revolution around  $x$  imposed by the spin-spin interaction, restricting its effect to a narrow region of solid angle  $\sim \pi/400\text{ sr}$  near the north pole.

Using a train of spin echos, we were able to further reduce these excessive magnetic field inhomogeneities by two orders of magnitude, to a negligible level. During their magnetic spin-spin evolution, the two dipoles were flipped at a rate of  $f_0 = 2\text{ Hz}$ . In geometric terms, this corresponds to a train of  $180^\circ$  rotations about the  $x$  axis (Fig. 1c). These collective rotations do not change the relative orientation of the spins, leaving the spin-spin interaction invariant (Fig. 1d, upper middle three spheres). The effect of the gradient, however, is averaged to zero because exchanging  $|\uparrow\downarrow\rangle$  and  $|\downarrow\uparrow\rangle$  is equivalent to constantly switching the sign

of the magnetic field gradient (Fig. 1d, lower middle three spheres). This scheme is an adaptation of the quantum lock-in method<sup>15</sup>.

We used parity analysis<sup>20</sup> to obtain a physical observable that is first-order sensitive to the interaction strength and the experiment time. The parity observable measures the coherence between  $|\uparrow\downarrow\rangle$  and  $|\downarrow\uparrow\rangle$ . To estimate it, we applied the following experimental sequence (Fig. 1d). The system state was initialized to  $|\uparrow\uparrow\rangle$  and then evolved under spin-spin interaction to  $|\psi(T)\rangle = \cos(2\xi T)|\uparrow\uparrow\rangle + i\sin(2\xi T)|\downarrow\downarrow\rangle$ . We then applied a controlled magnetic field gradient, adding a superposition phase  $\phi_{\text{parity}}$  to yield  $|\psi(T)\rangle = \cos(2\xi T)|\uparrow\uparrow\rangle + ie^{i\phi_{\text{parity}}}\sin(2\xi T)|\downarrow\downarrow\rangle$ . The expectation value of parity was then estimated as  $\langle\text{parity}\rangle = P_{\uparrow\uparrow} + P_{\downarrow\downarrow} - P_1$ , where  $P_{\uparrow\uparrow}$ ,  $P_{\downarrow\downarrow}$  and  $P_1 \equiv P_{\uparrow\downarrow} + P_{\downarrow\uparrow}$  are the probabilities of finding the system in the respective states, measured projectively after performing a collective  $\pi/2$  spin rotation (Supplementary Information). In this case,  $\langle\text{parity}\rangle = \sin(4\xi T)\sin(\phi_{\text{parity}})$ . The parity visibility,  $\sin(4\xi T)$ , is extracted either by scanning  $\phi_{\text{parity}}$  (Fig. 1e) or by setting it to  $\pi/2$ . Geometrically, parity corresponds to the projection of the Bloch vector on the  $x$  axis (Fig. 1d, rightmost sphere) and its visibility corresponds to the projection of the Bloch vector on the equatorial plane (Fig. 1c, black double arrow).

Measuring a weak, millihertz-scale, interaction requires an experiment duration of many seconds. Detection fidelity, however, deteriorates at these long times owing to ion motion heating, eventually limiting the experiment duration. As a result, the measured parity visibility reduces by a factor of  $\alpha = 1 - 4D(1 - D)$ , where  $D$  is the average of the  $|\uparrow\uparrow\rangle$  and  $|\downarrow\downarrow\rangle$  detection fidelities. Figure 2a shows the detection fidelities as a function of time for  $|\uparrow\uparrow\rangle$  and  $|\downarrow\downarrow\rangle$  at an inter-ion distance of  $d = 2.4\ \mu\text{m}$ . Although our measurement scheme was tailored to be first-order insensitive to heating, its residual effect degraded the detection fidelity from more than 0.95 at  $T = 5\text{ s}$  to as low as 0.88 at  $T = 25\text{ s}$ . These measurements are consistent with our measured heating rates, of  $\sim 10$  quanta per second. Asymmetry in the detection scheme accounts for the fidelity of the  $|\uparrow\uparrow\rangle$  measurement being better than that of the  $|\downarrow\downarrow\rangle$  measurement. Similar detection fidelities are displayed in Fig. 2b as functions of ion separation, for a fixed  $T = 15\text{ s}$  experiment time. As seen, detection

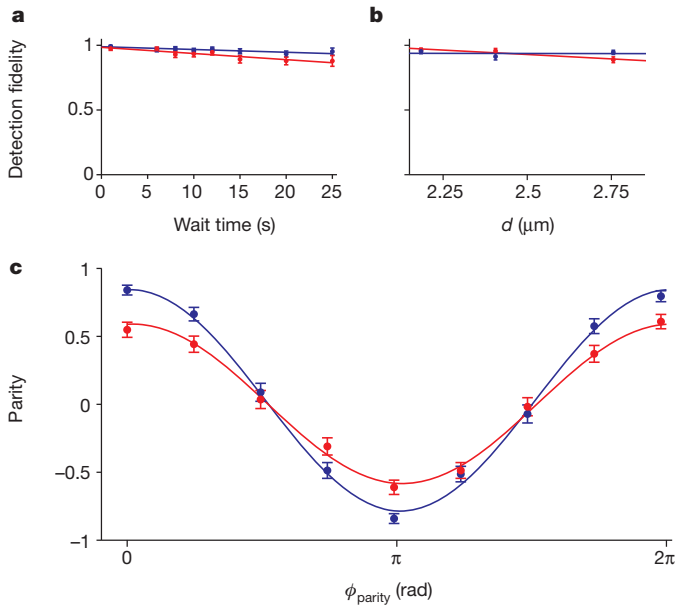


**Figure 2 | Characterization of quantum decoherence.** **a**, Detection fidelity versus experiment time for  $d = 2.4 \mu\text{m}$ . The probabilities of measuring  $|\uparrow\uparrow\rangle$  and  $|\downarrow\downarrow\rangle$  given that the system was initialized to  $|\uparrow\uparrow\rangle$  and, respectively,  $|\downarrow\downarrow\rangle$  are shown by the red and blue dots. Each point is the average of  $N = 119$  projective measurements. Solid lines are linear best fits. During the experiment, collective spin flips are applied at a period of 0.5 s as in the actual spin–spin experiment. Detection fidelities degrade owing to ion motion heating. **b**, Detection fidelity versus  $d$  for  $T = 15$  s (similar to **a**). The points at  $d = 2.18, 2.41, 2.76 \mu\text{m}$  are the averages of  $N = 147, 119, 201$  projective measurements, respectively. **c**, Dephasing time estimate. The system is initialized to  $|\Psi_+\rangle = (|\uparrow\downarrow\rangle + |\downarrow\uparrow\rangle)/\sqrt{2}$  and then a train of spin flips is applied as in **a** and **b**. Parity analysis is performed after respective wait times of  $T = 1$  s and 15 s, shown by the blue and red dots. Each point is the average of  $N = 226$  projective measurements. The blue and red lines are best fits to a cosine fringe, yielding respective amplitudes of  $0.81(5)$  and  $0.59(4)$  and a conservative estimate for the dephasing time of  $44 \pm 12$  s. When factoring out detection efficiency, we observe no statistically significant dephasing. All error bars indicate projection noise.

fidelity increases at lower inter-ion distances, corresponding to higher trap frequencies, where the effect of heating is known to be less pronounced<sup>11</sup>. A further, minor reduction in  $\alpha$  by a factor of  $>0.98$  is due to imperfect initialization. See Supplementary Information for a complete discussion of heating, detection and initialization as well as their effect on  $\alpha$ .

We limited our experiment duration to  $T = 15$  s, beyond which the decrease in  $\alpha$  compromises the increase in signal. Moreover, at the high trap voltages used, longer experiments resulted in a substantial ion loss from the trap owing to ion-crystal instabilities, thereby severely limiting the long averaging required to obtain statistical significance. The optimal 15-s duration chosen was still long enough for dephasing to potentially limit the observation of spin–spin interaction. Here dephasing within the DFS, for example due to residual noise in the magnetic field gradient, averages away the superposition relative phase between  $|\uparrow\downarrow\rangle$  and  $|\downarrow\uparrow\rangle$ . It results in a decreasing parity visibility as a function of time. To characterize this phase coherence, the system was initialized to  $|\Psi_+\rangle = (|\uparrow\downarrow\rangle + |\downarrow\uparrow\rangle)/\sqrt{2}$  using a Mølmer–Sørensen entangling gate<sup>21</sup>. This was followed by a wait of duration  $T$  while performing spin flips as in the actual spin–spin experiment, and ended with parity analysis. The state  $|\Psi_+\rangle$  was chosen because it is invariant under spin–spin coupling, while being sensitive to dephasing. Figure 2c displays the results for  $T = 1$  s and  $T = 15$  s using blue and red circles, respectively. A best fit to a cosine yields parity amplitudes of  $0.81(5)$  ( $T = 1$  s) and  $0.59(4)$  ( $T = 15$  s). A conservative estimate for coherence time, not taking detection fidelity into account, yields  $44 \pm 12$  s. Taking into account the degradation in detection, we cannot observe any statistically significant dephasing after 15 s.

We now turn to describing the main results of this letter. Figure 3 presents the parity measurements for two electronic spins undergoing magnetic dipolar interaction, at an inter-ion distance of  $d = 2.4 \mu\text{m}$ . A parity oscillation of  $\langle \text{parity} \rangle = \pm \alpha \sin(4\xi T) \sin(\phi_{\text{parity}})$  is expected, and will be positive when the initial state is  $|\uparrow\downarrow\rangle$  and negative for the initial state  $|\downarrow\uparrow\rangle$ . Figure 3a shows parity versus  $\phi_{\text{parity}}$  for  $T = 0.1$  s, which is much shorter than the spin–spin coupling timescale. As expected, no significant parity oscillation amplitude is detected. The  $T = 15$  s long-experiment results are shown in Fig. 3b. Here the parity sinusoidal dependence becomes evident. The solid blue and red lines are calculated from theory without any adjustable parameters, showing good agreement with the measured data. Shaded areas represent measurement uncertainties in determining  $\alpha$ . The theoretical interaction strength at the  $d = 2.4 \mu\text{m}$  distance is  $\xi = 2\pi \times 0.93$  mHz, in agreement with a single-parameter best fit of the data to the above theory yielding  $\xi = 2\pi \times 0.9(1)$  mHz. With the parity analysis sinusoidal dependence on  $\phi_{\text{parity}}$  established, the parity visibility can be measured by fixing  $\phi_{\text{parity}} = \pi/2$ , acquiring a single point rather than a complete sinusoidal fringe. In Fig. 3c we display visibility versus interaction time (blue circles), which is in agreement with the theoretical curve, visibility  $= \alpha \sin(4\xi T)$  (blue line).

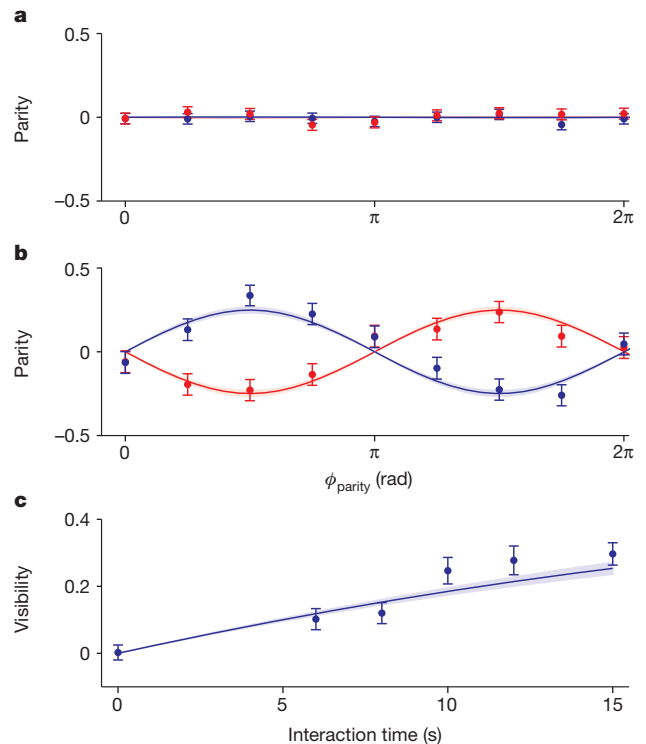


**Figure 3 | Coherent oscillations due to magnetic spin–spin interaction for  $d = 2.4 \mu\text{m}$ .** **a**, Parity analysis of a 0.1-s spin–spin experiment. Blue and red dots show parity measurements for the initial states  $|\uparrow\downarrow\rangle$  and  $|\downarrow\uparrow\rangle$ , respectively. Each point is the average of  $N = 945$  projective measurements. Solid lines are the spin–spin theory with no adjustable parameters, taking into account the preparation and detection fidelities, characterized in Fig. 2a. **b**, Same as Fig. 3a, for  $T = 15$  s. Each point is the average of  $N = 236$  projective measurements. Shaded areas are 1-s.d. intervals for the solid line theories, due to the uncertainties in characterizing the preparation and detection fidelities. A best fit to  $\alpha \sin(4\xi T) \sin(\phi_{\text{parity}})$  (not shown) yields an estimated coupling constant of  $\xi = 2\pi \times 0.9(1)$  mHz, in reasonable agreement with theory ( $\xi = 2\pi \times 0.93$  mHz). Here  $\alpha = 0.75$  is the visibility degradation factor, extracted from the data shown in Fig. 2a, as explained in the text. **c**, Parity amplitude (visibility) versus spin–spin interaction time,  $T$ . The parity observable is measured at  $\phi_{\text{parity}} = \pi/2$ . The points at  $T = 0, 6, 8, 10, 12, 15$  s are the averages of  $N = 2,001, 1,000, 1,000, 600, 501, 819$  projective measurements, respectively. Solid line and shaded area are the same as in **a** and **b**. A best fit to  $\alpha \sin(4\xi T)$  (not shown) yields  $\xi = 2\pi \times 1.1(2)$  mHz. All error bars indicate projection noise.

Although only partial entanglement is generated by spin–spin interaction after 15 s, it can still be observed by measuring a negative expectation value for a properly chosen entanglement witness<sup>22</sup>. Here we chose the swap operator, defined as swap  $|a, b\rangle = |b, a\rangle$  for any two single spin states  $|a\rangle$  and  $|b\rangle$ . In terms of the two spins' density matrix,  $\langle \text{swap} \rangle = P_{\uparrow\uparrow} + P_{\downarrow\downarrow} - \text{visibility}$ . Therefore, entanglement is proven by experimentally verifying that<sup>20</sup>  $P_{\uparrow\uparrow} + P_{\downarrow\downarrow} < \text{visibility}$ . We repeat the spin–spin experiment  $N = 2,388$  times, for  $d = 2.4 \mu\text{m}$ , measuring visibility = 0.28(2) and  $P_{\uparrow\uparrow} + P_{\downarrow\downarrow} = 0.11(1)$ . These conservative estimates, not taking the deterioration in detection fidelity into account, rendered the entanglement witness negative with good statistical significance:  $\langle \text{swap} \rangle = -0.16(2)$ . Here we assume a projection-noise-limited error in measured probabilities, supported by an Allen deviation analysis. Taking detection fidelity into account, using the calibration shown in Fig. 2a, our maximum-likelihood estimate renders  $\langle \text{swap} \rangle = -0.41(4)$ . See Supplementary Information for details of the maximum-likelihood estimation and the Allen deviation analysis.

Finally, the spin–spin interaction dependence on inter-electron distance is revealed by repeating the above measurement at different ion separations,  $d$ . Figure 4a shows the measured parity visibility (blue circles) versus  $d$ , in good agreement with theory (blue line): visibility =  $\alpha \sin(4\xi T)$ . Here  $\alpha$  is extracted from the data shown in Fig. 2b, and decreases from  $\alpha = 0.84$  at  $d = 2.18 \mu\text{m}$  to  $\alpha = 0.70$  at  $d = 2.76 \mu\text{m}$  owing to the larger motion heating rates at lower trap frequencies. The 64% decrease in the visibility is thus a combined effect of the 17% decrease in  $\alpha$  and the additional decrease in the spin–spin coupling constant,  $\xi$ .

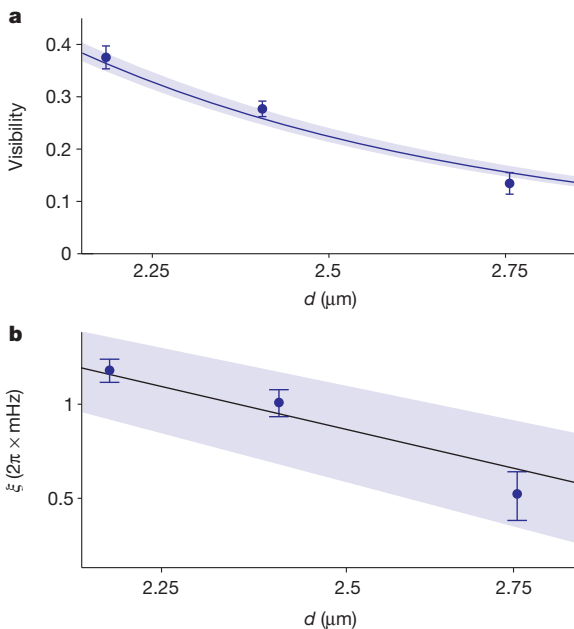


**Figure 4 | Magnetic spin–spin interaction as a function of distance.** **a**, Parity visibility versus ion separation,  $d$ , is shown by the blue dots for a fixed experiment time,  $T = 15$  s. The points at  $d = 2.18, 2.41, 2.76 \mu\text{m}$  are the averages of  $N = 2,306, 4,204, 1,796$  projective measurements, respectively. Error bars indicate projection noise. Solid line is spin–spin theory without adjustable parameters, taking preparation and detection fidelities into account, as characterized in Fig. 2b. Shaded blue area is a 1-s.d. interval for the solid line theory, due to the uncertainties in characterizing the preparation and detection fidelities. **b**, Spin–spin coupling strength  $\xi$  versus ion separation (log–log scale). Blue dots are extracted from **a**, using visibility =  $\alpha \sin(4\xi T)$ . The visibility degradation factor,  $\alpha$ , is extracted from the data in Fig. 2b. Error bars are 1-s.d. estimates due to projection noise in both the measurements and in the extraction of  $\alpha$ . The error bar for the  $d = 2.75 \mu\text{m}$  point is slightly larger owing to the corresponding decrease in  $\alpha$ . Solid black line is spin–spin theory without any adjustable parameters. A linear best fit to  $\xi = \mu_0(g\mu_B/2)^2/4\pi\hbar d^{-n}$  (not shown) yields  $n = 3.0(4)$ , consistent with the  $n = 3$  theoretical exponent. Shaded blue area indicates the  $n = 3.0 \pm 0.4$  curves.

We can therefore estimate  $\xi$ , using the measured parity visibility, and the independently measured  $\alpha$ , as shown in Fig. 4b (blue circles). A best fit to  $\xi = \mu_0(g\mu_B/2)^2/4\pi\hbar d^n$  yields  $n = 3.0(4)$ , in agreement with the cubic dependence of magnetic spin–spin interactions. Our apparatus allowed for a relatively small variation in  $d$ . Shorter distances required operating the trap at voltages higher than 400 V, where trap instabilities limited our integration efforts. Larger inter-ion separations resulted in a diminishing signal-to-noise ratio. Therefore, improving our measurement uncertainty requires a redesign of the ion trap, targeted at high-voltage operation.

Because the measured interaction is very weak, it requires ruling out competing spurious effects. Specifically, the ions' motion in the trap due to heating translates to a magnetic field in the ions' rest frame. Although this cannot lead to spin entanglement, it could contribute to the parity signal. However, because such a field would oscillate at trap frequencies which are all below 5 MHz, it would couple non-resonantly to the spins whose resonant frequency is  $\sim 13.16$  MHz. In Supplementary Information we quantitatively rule out this effect, as well as other possible competing phenomena. These include inter-ion distance fluctuations, quantization axis misalignment, radio-frequency electrode leakage and trap-electrode-generated magnetic field gradients.

We have used a combination of techniques, originally developed for the protection of quantum information, to measure the weak spin–spin magnetic interaction. Future improvements of this experiment may suggest a new platform for the exploration of anomalous spin forces<sup>23</sup> on the micrometre scale. The use of DFSS, which was central to our approach, is not restricted to the specifics of the reported experiment and they could be used in other metrological scenarios<sup>10,16</sup>. Quantum information processing continues to drive metrology with recent proposals<sup>24–27</sup> that harness quantum error correction for sensitive measurements.

## METHODS SUMMARY

Our apparatus enabled us to place the electronic spins at a controlled distance from one another, as well as to initialize, manipulate and detect their internal spin state with high fidelity. Details of the set-up are found in ref. 8 as well as in the Supplementary Information. Briefly, a Coulomb crystal of two ions was formed in an electrical Paul trap<sup>9</sup> with Doppler cooling. We used external voltages to push the ions against their Coulomb repulsion (Fig. 1a), thus controlling the inter-ion separation,  $d$ . The minimal distance attained was limited by our ability to maintain stable ion crystals without incurring a trap voltage breakdown. The inter-ion distance is the difference between the equilibrium positions of two charged particles trapped in a harmonic trap,  $d = (2k_e e^2 / M(2\pi f_{\text{trap}})^2)^{1/3}$ , where  $k_e$  is Coulomb's constant,  $e$  is the electron charge and  $M$  is the mass of  $^{88}\text{Sr}^+$ . The oscillation frequency,  $f_{\text{trap}}$ , was measured spectroscopically. For  $^{88}\text{Sr}^+$ , the valence electron spin states are  $|\uparrow\rangle = |5s_{1/2}, J = 1/2, M_J = 1/2\rangle$  and  $|\downarrow\rangle = |5s_{1/2}, J = 1/2, M_J = -1/2\rangle$ . State initialization to  $|\uparrow\uparrow\rangle$  was done by optical pumping. We were able to perform all possible collective spin rotations by pulsing a resonant radio-frequency magnetic field and tuning the pulse duration and the radio-frequency field phase. State detection was performed by state-selective fluorescence, distinguishing  $|\uparrow\uparrow\rangle$  and  $|\downarrow\downarrow\rangle$  from one another and from both  $|\uparrow\downarrow\rangle$  and  $|\downarrow\uparrow\rangle$ , which were indistinguishable<sup>28</sup>. All these collective operations had typical fidelities of more than 98%. We used inhomogeneities in the ion trap potential to perform differential spin rotations<sup>29,30</sup>, and were able to generate, for example,  $|\uparrow\downarrow\rangle$  with a typical fidelity of more than 98%. Finally, we were able to generate the entangled states  $|\Psi_{\pm}\rangle = (|\uparrow\downarrow\rangle \pm |\downarrow\uparrow\rangle) / \sqrt{2}$  using a Molmer–Sørensen entangling gate with a typical fidelity of 95% (ref. 21).

Received 16 December 2013; accepted 15 April 2014.

- Budker, D., Kimball, D. F. & DeMille, D. P. (eds) *Atomic Physics: An Exploration through Problems and Solutions* 1–50 (Oxford Univ. Press, 2004).
- Stuhler, J. *et al.* Observation of dipole-dipole interaction in a degenerate quantum gas. *Phys. Rev. Lett.* **95**, 150406 (2005).
- Lu, M., Burdick, N. Q., Youn, S. H. & Lev, B. L. Strongly dipolar Bose-Einstein condensate of dysprosium. *Phys. Rev. Lett.* **107**, 190401 (2011).
- Dolde, F. *et al.* Room-temperature entanglement between single defect spins in diamond. *Nature Phys.* **9**, 139–143 (2013).
- Grinolds, M. S. *et al.* Nanoscale magnetic imaging of a single electron spin under ambient conditions. *Nature Phys.* **9**, 215–219 (2013).
- Rugar, D., Budakian, R., Mamin, H. & Chui, B. Single spin detection by magnetic resonance force microscopy. *Nature* **430**, 329–332 (2004).
- Hanneke, D., Fogwell, S. & Gabrielse, G. New measurement of the electron magnetic moment and the fine structure constant. *Phys. Rev. Lett.* **100**, 120801 (2008).

8. Akerman, N., Glickman, Y., Kotler, S., Keselman, A. & Ozeri, R. Quantum control of  $^{88}\text{Sr}^+$  in a miniature linear Paul trap. *Appl. Phys. B* **107**, 1167–1174 (2012).
9. Wineland, D. *et al.* Experimental issues in coherent quantum-state manipulation of trapped atomic ions. *J. Res. Natl. Inst. Stand. Technol.* **103**, 259–328 (1998).
10. Roos, C. F., Chwalla, M., Kim, K., Riebe, M. & Blatt, R. 'Designer atoms' for quantum metrology. *Nature* **443**, 316–319 (2006).
11. Turchette, Q. A. *et al.* Heating of trapped ions from the quantum ground state. *Phys. Rev. A* **61**, 063418 (2000).
12. Biercuk, M. J., Uys, H., Britton, J. W., VanDevender, A. P. & Bollinger, J. J. Ultrasensitive detection of force and displacement using trapped ions. *Nature Nanotechnol.* **5**, 646–650 (2010).
13. Roos, C. F. *et al.* Bell states of atoms with ultralong lifetimes and their tomographic state analysis. *Phys. Rev. Lett.* **92**, 220402 (2004).
14. Langer, C. *et al.* Long-lived qubit memory using atomic ions. *Phys. Rev. Lett.* **95**, 060502 (2005).
15. Kotler, S., Akerman, N., Glickman, Y., Keselman, A. & Ozeri, R. Single-ion quantum lock-in amplifier. *Nature* **473**, 61–65 (2011).
16. Schmidt-Kaler, F. & Gerritsma, R. Entangled states of trapped ions allow measuring the magnetic field gradient produced by a single atomic spin. *Europhys. Lett.* **99**, 53001 (2012).
17. Kotler, S., Akerman, N., Glickman, Y. & Ozeri, R. Nonlinear single-spin spectrum analyzer. *Phys. Rev. Lett.* **110**, 110503 (2013).
18. Chou, C. W., Hume, D. B., Rosenband, T. & Wineland, D. J. Optical clocks and relativity. *Science* **329**, 1630–1633 (2010).
19. Breit, G. The magnetic moment of the electron. *Nature* **122**, 649 (1928).
20. Sackett, C. A. *et al.* Experimental entanglement of four particles. *Nature* **404**, 256–259 (2000).
21. Navon, N. *et al.* Quantum process tomography of a Mølmer-Sørensen interaction. Preprint at <http://arxiv.org/abs/1309.4502> (2013).
22. Horodecki, M., Horodecki, P. & Horodecki, R. Separability of mixed states: necessary and sufficient conditions. *Phys. Lett. A* **223**, 1–8 (1996).
23. Moody, J. E. & Wilczek, F. New macroscopic forces? *Phys. Rev. D* **30**, 130–138 (1984).
24. Ozeri, R. Heisenberg limited metrology using quantum error-correction codes. Preprint at <http://arxiv.org/abs/1310.3432> (2013).
25. Arrad, G., Vinkler, Y., Aharonov, D. & Retzker, A. Increasing sensing resolution with error correction. *Phys. Rev. Lett.* **112**, 150801 (2014).
26. Kessler, E. M. *et al.* Quantum error correction for metrology. *Phys. Rev. Lett.* **112**, 150802 (2014).
27. Dür, W., Skotiniotis, M., Fröwis, F. & Kraus, B. Improved quantum metrology using quantum error correction. *Phys. Rev. Lett.* **112**, 080801 (2014).
28. Keselman, A., Glickman, Y., Akerman, N., Kotler, S. & Ozeri, R. High-fidelity state detection and tomography of a single-ion Zeeman qubit. *New J. Phys.* **13**, 073027 (2011).
29. Warring, U. *et al.* Individual-ion addressing with microwave field gradients. *Phys. Rev. Lett.* **110**, 173002 (2013).
30. Navon, N. *et al.* Addressing two-level systems variably coupled to an oscillating field. *Phys. Rev. Lett.* **111**, 073001 (2013).

**Supplementary Information** is available in the online version of the paper.

**Acknowledgements** We thank J. Avron for discussions on the entanglement witness. We acknowledge support by the Israeli Science Foundation, the Crown Photonics Center, the German-Israeli Science Foundation and M. Kushner Schnur, Mexico.

**Author Contributions** S.K. designed the scheme for measuring spin–spin coupling. S.K. and N.A. performed the measurements. S.K. analysed the results. S.K., N.A., N.N. and Y.G. developed the techniques necessary to experimentally implement the measurement scheme. S.K. and R.O. wrote the paper. R.O. supervised the work. All authors discussed the results and contributed to the manuscript.

**Author Information** Reprints and permissions information is available at [www.nature.com/reprints](http://www.nature.com/reprints). The authors declare no competing financial interests. Readers are welcome to comment on the online version of the paper. Correspondence and requests for materials should be addressed to S.K. ([shlomi.kotler@weizmann.ac.il](mailto:shlomi.kotler@weizmann.ac.il)).